



Article

Shaking-Table Test and Finite Element Simulation of a Novel Friction Energy-Dissipating Braced Frame

Lijuan Yan ^{1,2}  and Chunwei Zhang ^{1,3,*} 

¹ School of Civil Engineering, Qingdao University of Technology, Qingdao 266033, China; lijuan.yan@qdc.edu.cn

² School of Civil Engineering, Qingdao City University, Qingdao 266100, China

³ School of Marine Science and Engineering, South China University of Technology, Guangzhou 511442, China

* Correspondence: zhangchunwei@scut.edu.cn

Abstract: To enhance the effect of seismic mitigation in medium-sized buildings, this study introduced a novel friction damper within a braced frame, forming a friction energy-dissipating braced frame (FDBF). The seismic reduction mechanism of the FDBF was examined, and its performance was evaluated through shaking-table tests and finite element simulations. The hysteresis performance of the novel damper was assessed through low-cycle repeated loading tests, which yielded predominantly rectangular and full hysteresis curves, exemplifying robust energy dissipation capacity. The shaking-table tests of the FDBF indicated significant modifications in the dynamic characteristics of the original frame structure, which notably reduced the natural vibration period and enhanced the damping. Additionally, the FDBF remarkably reduced both acceleration and displacement responses during seismic excitation. Optimizing the orientation of the energy dissipation brace significantly improved seismic reduction efficiency. A dynamic time history analysis, employing finite element software, was conducted on the FDBF equipped with a friction energy dissipation brace at each level. Comparative analysis with both the moment-resistant frame and ordinary braced frame revealed that the FDBF substantially lowered the peak acceleration at the apex of the structure, achieving a reduction rate of 40–50%. Under both design and rare earthquake conditions, the FDBF demonstrated superior seismic mitigation capabilities, especially under rare earthquakes. Future studies should investigate various structural types with energy dissipation braces at different levels to identify the most efficient layout for the novel friction energy dissipation brace, thereby guiding relevant engineering practices.

Keywords: novel friction damper; energy-dissipating brace; shaking-table test; finite element simulation



Citation: Yan, L.; Zhang, C. Shaking-Table Test and Finite Element Simulation of a Novel Friction Energy-Dissipating Braced Frame. *Buildings* **2024**, *14*, 390. <https://doi.org/10.3390/buildings14020390>

Academic Editors: Xinxin Wei, Daniele Perrone, Xinzhi Dang, Zhihao Wang, Junfeng Jia and Murat Dicleli

Received: 18 December 2023

Revised: 17 January 2024

Accepted: 24 January 2024

Published: 1 February 2024



Copyright: © 2024 by the authors. Licensee MDPI, Basel, Switzerland. This article is an open access article distributed under the terms and conditions of the Creative Commons Attribution (CC BY) license (<https://creativecommons.org/licenses/by/4.0/>).

1. Introduction

Frame structures are prevalently applied in medium- and high-rise buildings, as they provide clear force transmission pathways, flexible design, and cost-effectiveness. However, their significant limitation lies in lateral stiffness, which impedes effective interval displacement control during seismic events owing to inherent stiffness. Frame structures primarily address seismic impacts through the plastic deformation of their key structural components, which may induce permanent damage and reduce the overall seismic resilience [1]. In addressing this issue, numerous researchers have integrated energy-dissipating elements to absorb seismic forces, thus protecting the primary structure. The design philosophy of “moderate lateral stiffness with predominant energy dissipation through non-structural elements” [2,3] has evolved and become increasingly popular. A prominent example of this approach is the friction energy dissipation braced-frame structure.

In 1982, Pall and Marsh introduced the Pall-type friction energy-dissipation brace, featuring a four-link variable mechanism at the center to prevent buckling under horizontal seismic forces. This design facilitates energy dissipation through friction by incorporating

a slide groove at the midpoint of the diagonal [3–5]. In 1985, Chen devised a friction shear hinge energy-dissipation brace, employing friction shear dampers at diagonal brace intersections [6,7]. Extensive subsequent research by Liu [8,9] and Zhou [10,11] led to the development of circular (square box) friction energy dissipation braces. These designs replaced the Pall-type four-link mechanism with a circular ring or square box, placing the friction damper at the center of the diagonal for energy dissipation [8–12]. Xian et al. [13,14] proposed a composite friction energy-dissipating brace, combining sliding friction dampers at the diagonal's center with rotating friction dampers at the four link corners. In 2003, Ou and Wu et al. [15–17] introduced a T-shaped core plate friction damper, an advancement of the Pall-type damper, substituting diagonal cross-shaped bars with T-shaped core plates.

The friction dampers previously mentioned are typically installed in the central section of diagonal braces and come in various forms. These dampers employ sliding friction for energy dissipation. However, their complex construction can increase the axial force on columns due to horizontal seismic forces [16,18,19]. This paper introduces a novel friction energy-dissipating braced frame (FDBF), as illustrated in Figure 1. The FDBF comprises a frame structure and an innovative friction-based energy-dissipating brace, featuring a new type of friction damper and braces.

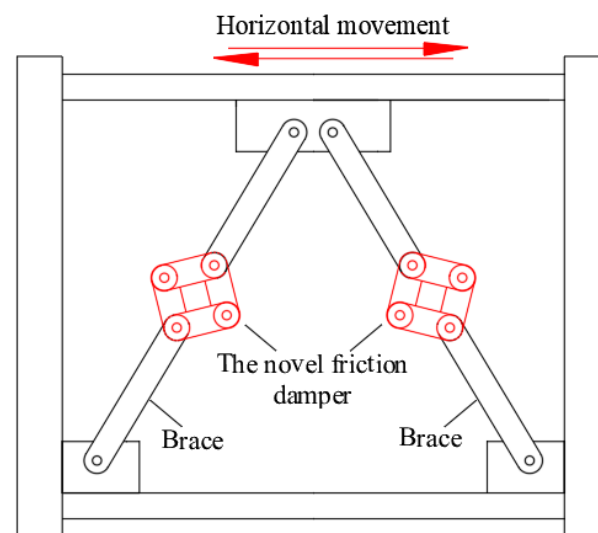


Figure 1. Novel friction energy-dissipating braced frame.

When subjected to horizontal seismic forces, the braces experience axial tension and compression, activating the damper. This leads to friction energy dissipation once the axial force reaches the slip force threshold of the new friction damper. The dissipation process involves the relative rotation of the connecting components and the friction pad, effectively reducing the displacement response of the structure during seismic events. The slip mechanism of the damper, designed to prevent compression buckling of the brace, allows the novel friction damper to adjust the absorbed length of the brace by deforming, keeping the slip force relatively constant despite increasing deformation. This design minimizes the additional axial force imparted to the column, thereby avoiding a gradual increase in column axial force. Additionally, this system offers several advantages, including straightforward construction, ease of installation, and flexibility, highlighting its practicality for seismic mitigation.

This article introduces and empirically investigates the working mechanism and hysteretic behavior of a new type of friction damper. Additionally, shaking-table tests and finite element simulations are conducted on the FDBF. The dynamic characteristics and seismic mitigation effects of the FDBF are thoroughly analyzed and assessed.

2. Study on Hysteretic Performance of the Novel Friction Damper

2.1. Theoretical Study

The innovative friction damper consists of six key components: a connecting plate, friction pad, steel disc, bolt washer, general bolts, and high-strength bolts, as illustrated in Figure 2. At the energy-dissipation end of the damper, each friction pad is securely attached using two connectors and fastened with high-tensile bolts under pre-pressure. To enable rotational movement between connectors at the loading end of the damper in response to external forces, ordinary discs, fixed with general bolts, are utilized in lieu of friction pads. Moreover, to modulate the energy-dissipating capacity of the friction pads, the steel disc at the loading end can be treated with a lubricant coating.

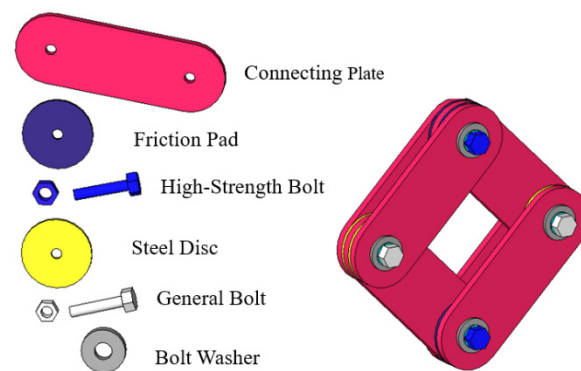


Figure 2. Novel friction damper construction.

Figure 3a,b illustrate the positive ($\Delta \geq 0$, Δ ranging from 0 to the maximum value and from the maximum value to 0) and negative ($\Delta < 0$, Δ ranging from 0 to the negative maximum value and from the negative maximum value to 0) displacements of the damper. These diagrams show that when a force, F , is applied to the loading end of the damper, relative rotation occurs between the connecting components and friction pads of the damper, causing frictional energy dissipation. As depicted in Figure 4, we can obtain: $x = L \sin \varphi$, then $dx = L \cos \varphi d\varphi$. Assuming that the displacement at the B (C) end of the damper is Δ ($dx = \Delta$) and the rotation angle of the damper is $\Delta\varphi$ ($d\varphi = \Delta\varphi$), we can obtain Equation (1) according to the principle of virtual work [20,21]:

$$2F\Delta = nM \cdot 2\Delta\varphi \quad (1)$$

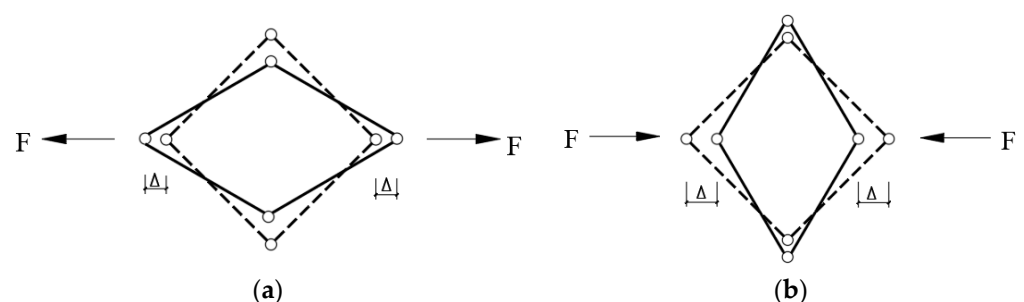


Figure 3. Mechanical model of damper.

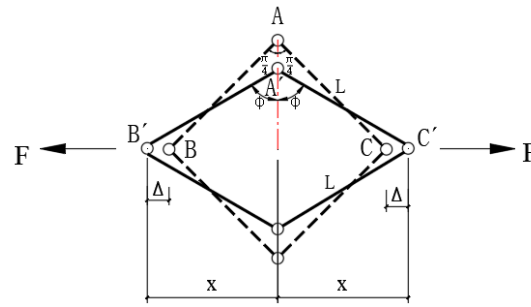


Figure 4. Stress diagram of isolator (positive).

Equation (2) can be obtained by substituting $\Delta = L \cos \varphi \cdot \Delta\varphi$ into Equation (1):

$$F = \frac{nM}{L \cos \varphi} \tag{2}$$

where M denotes the friction moment at the energy dissipation end of the damper, and n denotes the number of friction pads. The working principle of the friction pad is illustrated in Figure 5. When the rotational angle of the connecting plates is $\Delta\varphi$, the rotational angle of the friction pad is $\Delta\varphi$, and Equation (3) can be derived.

$$M = \iint \mu p c r^2 d\varphi dr = \frac{2}{3} \mu P \frac{R_2^3 - R_1^3}{R_2^2 - R_1^2} \tag{3}$$

where P denotes the preload force of high-strength bolts, μ indicates the friction coefficient of the friction pads, n represents the number of friction pads, and R_1 and R_2 denote the inner and outer radii of the friction pads, respectively.

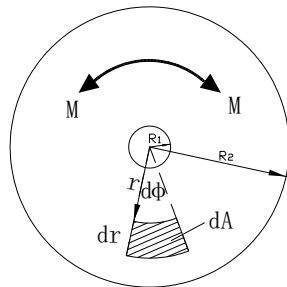


Figure 5. Working principle of friction pad.

Substituting Equation (3) into Equation (2), the theoretical formula for $F-\Delta$ is obtained for $\Delta \geq 0$ as follows:

$$F = \frac{2}{3L} n \mu P \frac{R_2^3 - R_1^3}{R_2^2 - R_1^2} / \sqrt{1 - \left(\frac{\sqrt{2}}{2} + \frac{\Delta}{L}\right)^2} \tag{4}$$

Similarly, Equation (5) can be obtained for $\Delta < 0$ as follows:

$$F = \frac{2}{3L} n \mu P \frac{R_2^3 - R_1^3}{R_2^2 - R_1^2} / \sqrt{1 - \left(\frac{\sqrt{2}}{2} - \frac{\Delta}{L}\right)^2} \tag{5}$$

From Equations (4) and (5), the theoretical $F-\Delta$ relationship of the novel friction damper is obtained, as displayed in Figure 6.

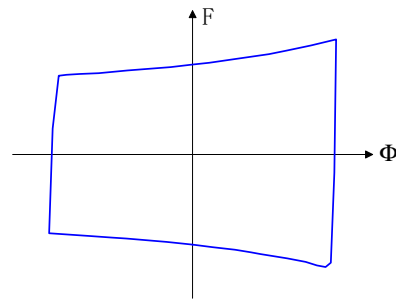


Figure 6. Theoretical hysteresis curve of $F-\Delta$.

2.2. Experimental Study

2.2.1. Specimen Design

To more accurately replicate the actual performance of the new friction damper through a hysteresis curve, a reverse-cycle loading test was conducted at the structural laboratory of Qingdao University of Technology. Six specimen sets were designed, varying in preloading forces of high-strength bolts and friction pad materials, as detailed in Table 1. The specimens utilized grade 8.8 M12 high-strength bolts and Q345 steel for other damper components. According to the JGJ 82-2011 “Technical Specification for High-Strength Bolt Connections of Steel Structures” and the predetermined test conditions [22–25], the preloading force P of the high-strength bolts was set at 38 kN. The specimen identifiers were structured as follows: RFD-friction pad material-preloading force magnitude, with “N” representing non-asbestos composite material, “A” asbestos composite material, and “B” brass.

Table 1. Specimen parameters.

Specimens	Friction Pad Type	Pre-Tension (kN)	Torque (kN·m)
RFD-NA-0.5P	Non-asbestos composite	0.5P	0.78P
RFD-NA-P	Non-asbestos compound	P	1.56P
RFD-A-0.5P	Asbestos compound	0.5P	0.78P
RFD-A-P	Asbestos compound	P	1.56P
RFD-B-0.5P	Brass	0.5P	0.78P
RFD-B-P	Brass	P	1.56P

As depicted in Figure 7, the geometrical dimensions of all six sets of specimens were identical.

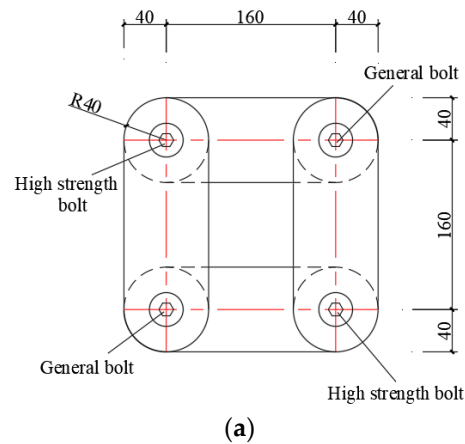


Figure 7. Cont.

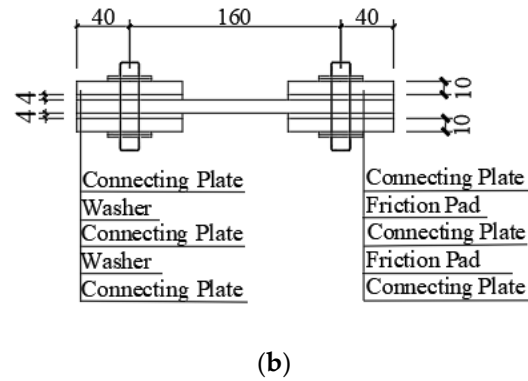


Figure 7. Geometric dimensions of specimens. (a) Elevation. (b) Side view.

2.2.2. Experimental Equipment and Loading Protocol

A 100-kN hydraulic servo loading MTS actuator, specifically engineered for horizontal linear loading, was employed in the experiment. One extremity of the square rotary friction damper was connected to the actuator, whereas the opposite end was linked to a limiting device. The MTS force and displacement sensors were used for real-time data collection. The loading apparatus is displayed in Figure 8a, and the experimental loading methodology is illustrated in Figure 8b. The displacement-controlled loading was adopted, and Figure 9 presents the test loading protocol.

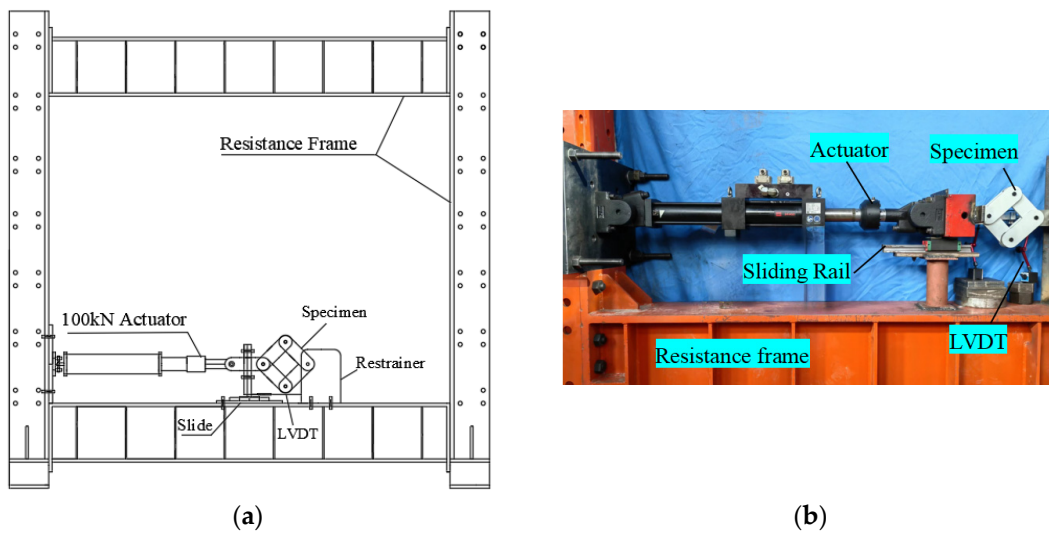


Figure 8. Loading diagram and device.(a) Loading diagram. (b) Loading device.

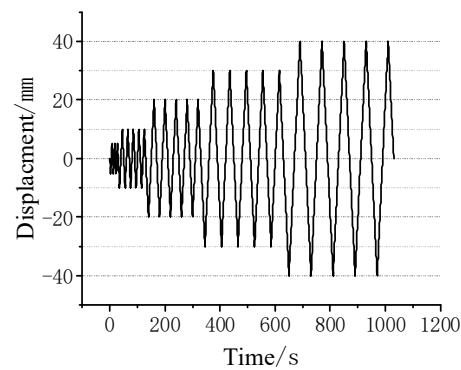


Figure 9. Loading protocol.

2.2.3. Experimental Results and Analysis

The primary parameters measured in this experiment included the displacement of the novel friction damper, the differential in displacement between the damper and the limit fixing device, and the variation in the sliding force of the damper. The displacement was quantified using displacement sensors, whereas the sliding force of the friction damper was measured using the force sensor of the actuator. These measurements facilitated the construction of the hysteresis curve of the friction damper, as depicted in Figure 10. This curve was predominantly rectangular and full. Even after 25 reciprocating displacement loading cycles, there was no significant degradation in stiffness, highlighting the robust energy-dissipation capacity of the damper. Moreover, the hysteresis curve of the damper was closely aligned with the theoretical analysis presented in Figure 6, affirming the general accuracy of the theoretical formula.

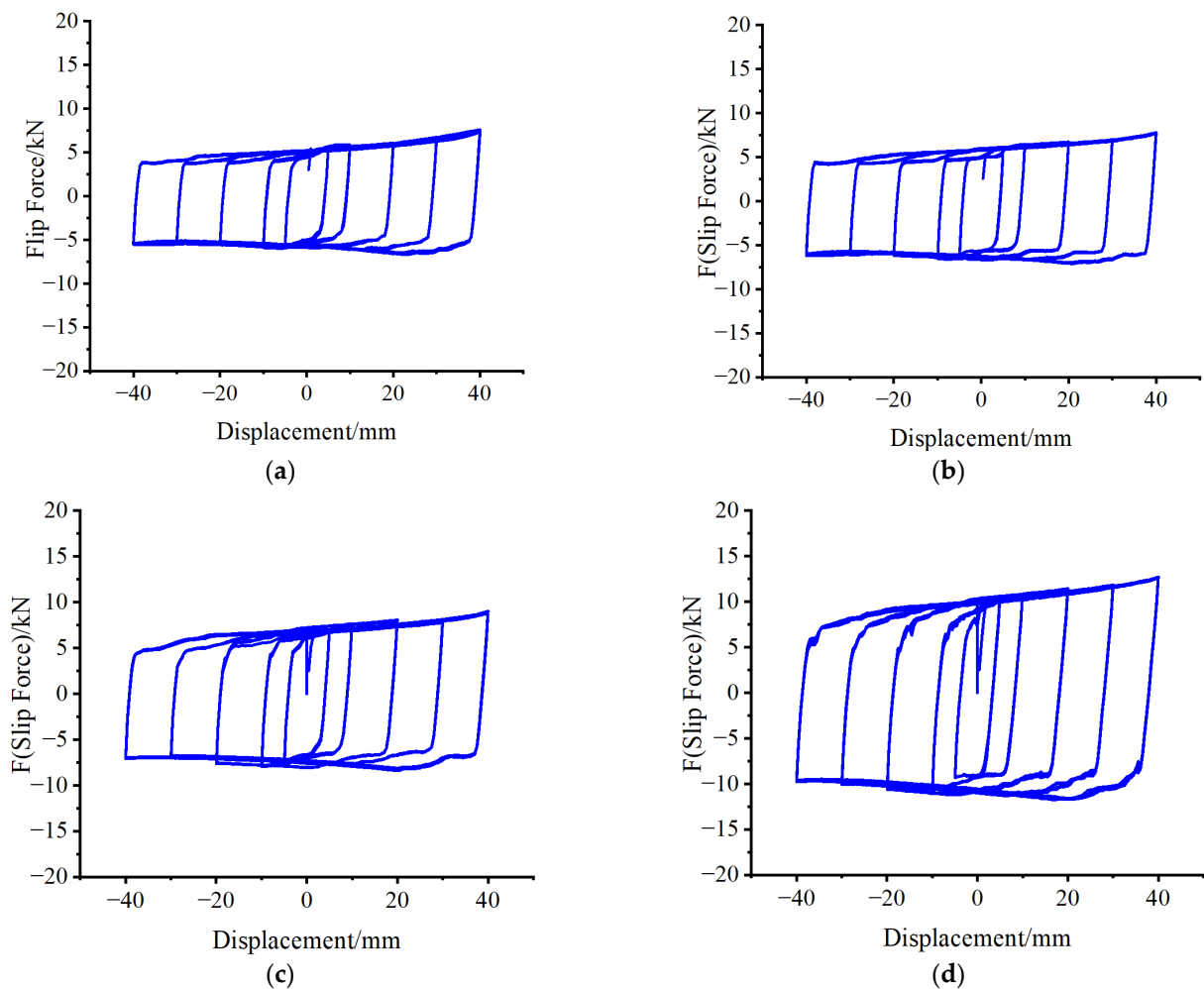


Figure 10. Cont.

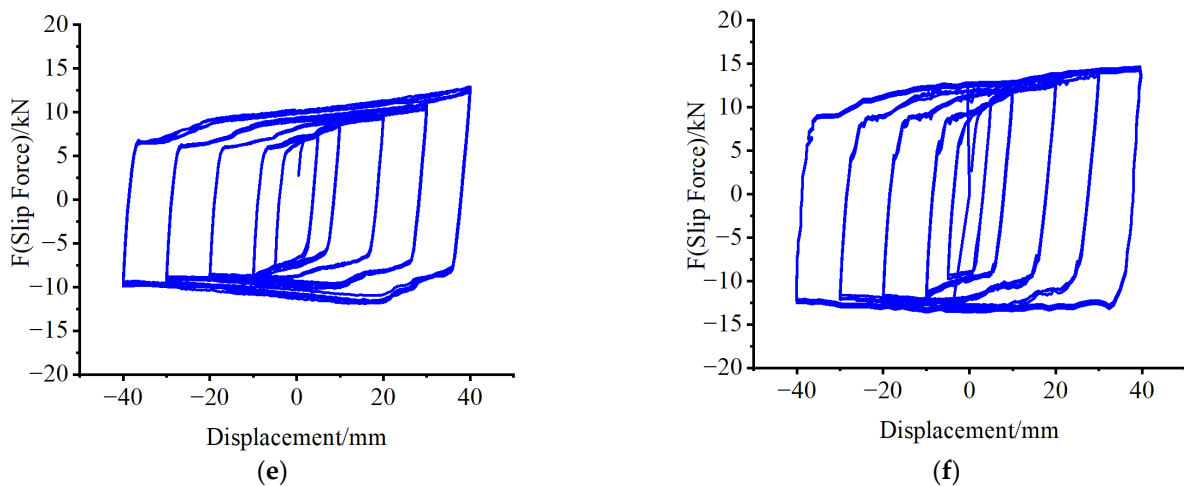


Figure 10. Hysteresis curves. (a) RFD-NA-0.5P. (b) RFD-NA-P. (c) RFD-A-0.5P. (d) RFD-A-P. (e) RFD-B-0.5P. (f) RFD-B-P.

The sliding force F of the friction damper increases with a rise in the preloading force of the bolts, assuming constant friction-pad material. With identical preloading forces, the sliding force is minimized with non-asbestos composite material friction pads and maximized with brass. Therefore, the sliding force of the friction damper is influenced by both the preloading force of the bolts and the friction coefficient of the friction pad. Thus, different energy-dissipation capacities can be achieved by varying the preloading force of the bolts or employing different friction-pad materials for friction energy dissipation.

3. Study on Novel Friction Energy-Dissipating Braced Frame

3.1. Theoretical Study

Incorporating the friction damper into braces leads to the creation of a friction-based energy-dissipation structural system. Under horizontal seismic action, a mechanical analysis of the single-layer seismic damping structure can be performed, as depicted in Figure 1. This analysis produces a simplified diagram, displayed in Figure 11a, which divides the system into a single-layer frame structure and a dampening support section incorporating the damper. Figure 11b displays the energy-dissipation support, integrating the friction damper to augment energy dissipation and enhance the seismic performance of the structure.

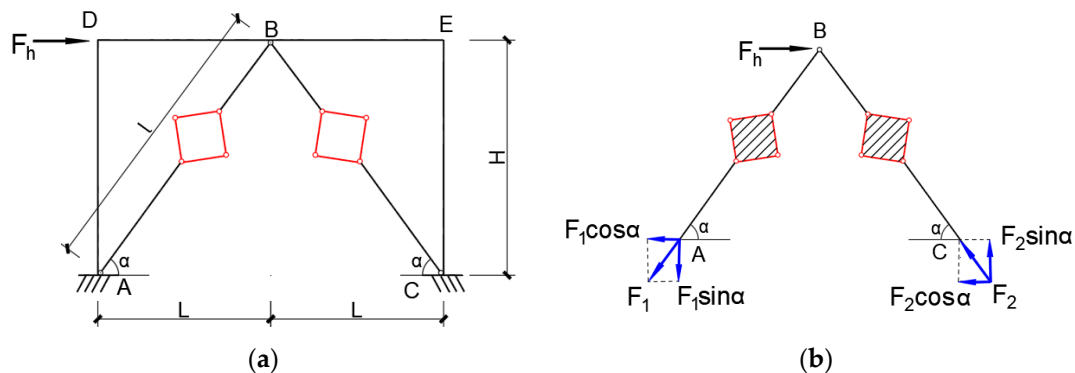


Figure 11. Calculation diagrams and the brace. (a) Friction energy dissipating-braced frame. (b) Friction energy dissipating-brace.

When subjected to mild horizontal seismic forces, as indicated in Figure 11a, the AB rod remains in tension without deformation, whereas the AC rod experiences compression without collapsing. The energy-dissipation end of the friction damper remains static, and the energy-dissipation support is in an elastic stage. At this stage, the friction damper

functions as a rigid body, rendering the energy-dissipation support similar to a conventional support. According to the principles of structural mechanics, the primary function of the support is to withstand the horizontal force [26–28].

$$F_1 = F_2 \quad (6)$$

$$F_h = F_1 \cos \alpha + F_2 \cos \alpha \quad (7)$$

When Equation (6) is substituted into Equation (7), we obtain $F_1 = \frac{1}{2 \cos \alpha} F_h$. Following the same reasoning, we can obtain $F_2 = \frac{1}{2 \cos \alpha} F_h$.

As the horizontal seismic force intensifies to a level where the AC compression support approaches buckling, the novel friction damper starts to rotate and engage, as illustrated in Figure 12. At this moment, the sliding force of the damper attains its maximum friction force. The internal force within the brace, provided by the support, can be computed as follows:

$$F_{sl} = \frac{1}{2 \cos \alpha} F_h \quad (8)$$

$$F_{sl} = \varphi A_b f_y \quad (9)$$

where φ denotes the stability coefficient of the compression support, A_b represents the cross-sectional area of the compression support, and f_y indicates the design value of the compressive strength of the steel material used for the support.

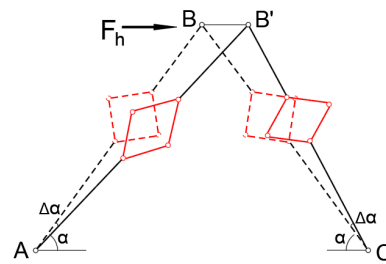


Figure 12. Energy-dissipating brace operation.

3.2. Shaking-Table Test

The experimental prototype is based on the initial-stage ATS-controlled benchmark model, incorporating studies [29–33]. It is a three-story, single-span steel-frame structure. The scaled-down model employed in this experiment has dimensions of 366 mm by 183 mm in plan, with a first-story height of 305 mm and subsequent stories each measuring 448 mm. The friction damper energy-dissipation brace was installed on the first story. The columns comprised 13 circular cylinders, and the base plate was firmly bolted to the shaking table. To adhere to the similarity criteria of the structural model, the friction damper was re-engineered, with dimensions presented in Figure 13. The frame model specimens were constructed according to the dimensions of each component, and the FDBF model specimens are exhibited in Figure 14.

3.2.1. Test Equipment and Loading Scheme

For the experiment, the Quanser Shake Table III, a bi-axial input vibration table measuring 71.1 cm × 71.1 cm, was utilized. Capable of handling a 100 kg load, it can generate a maximum seismic excitation level of 1 g. Both the X and Y directions have a stroke capability of 10.8 cm. Acceleration data were acquired using four Lord G-Link-200 sensors placed on the surface of the shaking table and at the center of each floor slab. Structural displacement signals were measured using Keyence CMOS IL series laser displacement sensors. The seismic performance was evaluated by comparing the lateral displacement and acceleration of both the FDBF and moment-resistant frame (MRF). The design response spectrum was formulated based on seismic intensity, site classification, and seismic design category, with the seismic intensity set at 8 degrees, site classification at

Class II, and seismic design category at Group 2. The resulting design response spectrum is depicted in Figure 15.

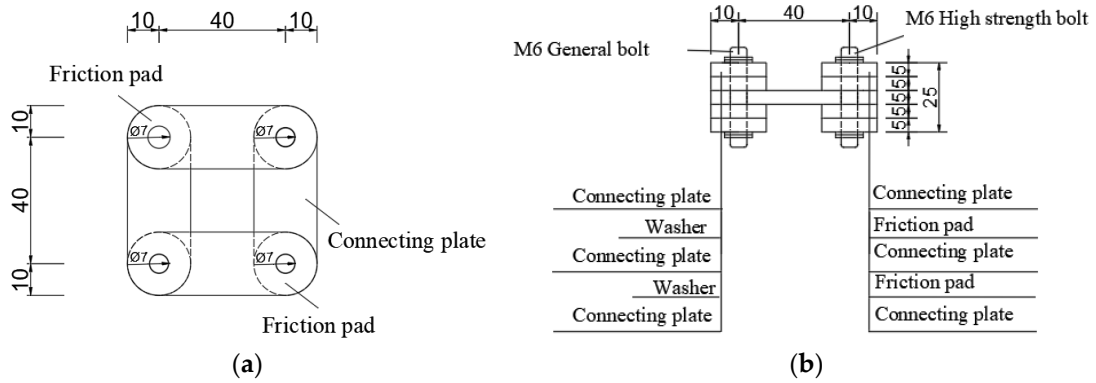


Figure 13. Design details of the table-test friction damper model. (a) Elevation. (b) Side view.

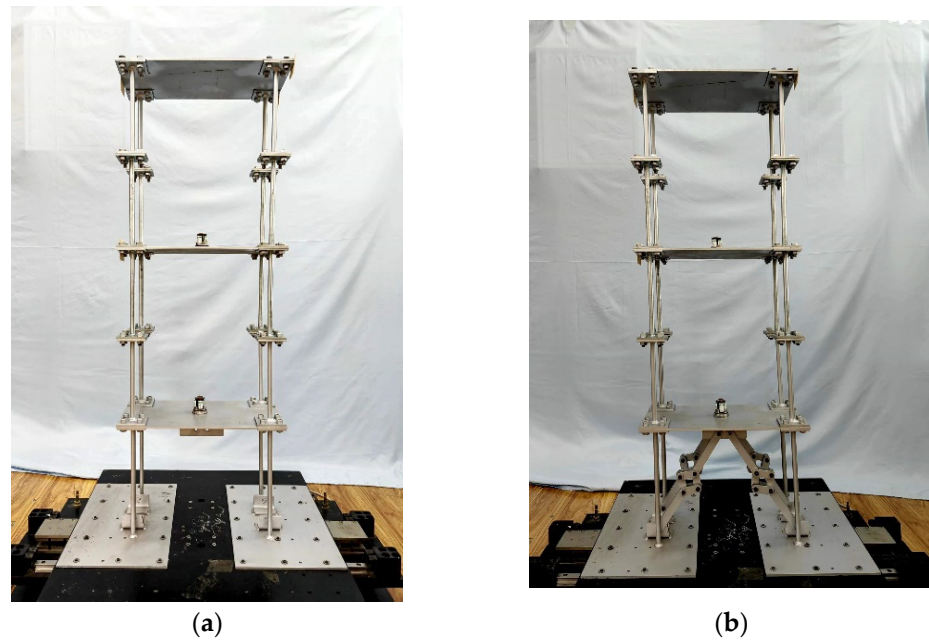


Figure 14. Model specimens. (a) Frame model specimen. (b) Friction damper braced frame specimen.

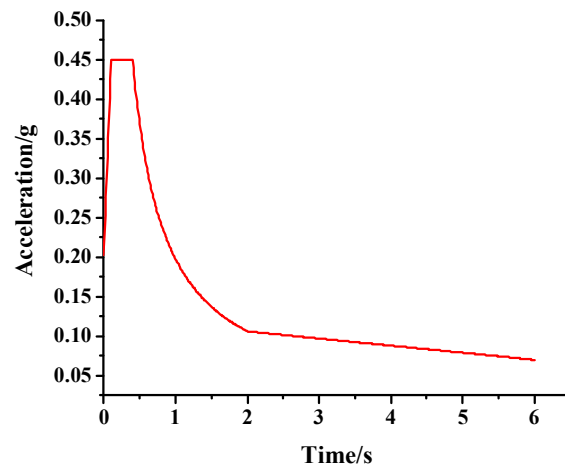


Figure 15. Design earthquake response spectrum.

Four seismic waves—the 1940 El Centro wave, 1979 El Centro wave, 1981 Salton Sea wave, and 1952 Taft wave—were selected for their spectral congruence with the structural period point. The peak values of these waves were adjusted to 0.2 g. A response spectrum analysis for each wave was then conducted and compared with the response spectrum from Code for Seismic Design of Buildings GB50011–2010(2016 Edition), as illustrated in Figure 16. The response spectra of these waves closely corresponded with the periods of the structure. The average response values of these waves were used to assess the seismic performance of the structure [34,35]. Owing to structural asymmetry, earthquake waves were applied independently in the X and Y directions. The structural model loading device is depicted in Figure 17.

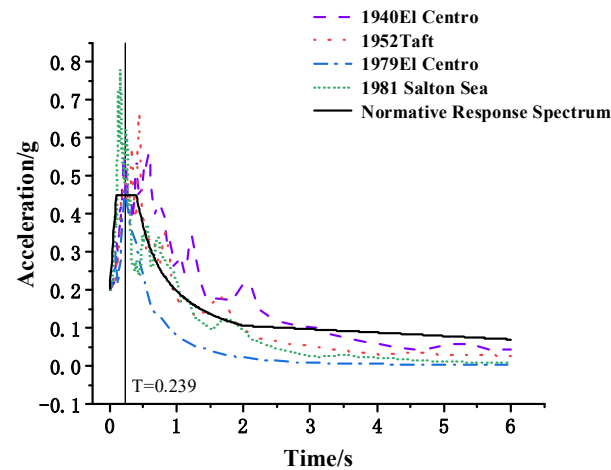


Figure 16. Earthquake wave response spectrum and design response spectrum.

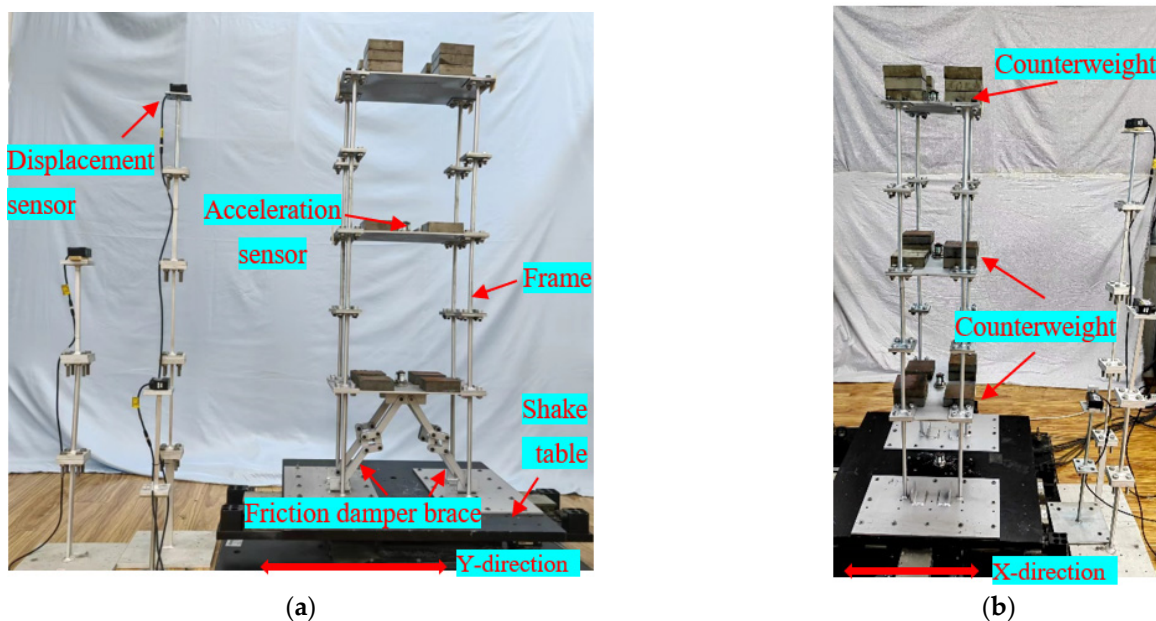


Figure 17. Loading device for the structural model specimens (a) Loading device in Y-direction. (b) Loading device in X-direction.

3.2.2. Test Results and Analysis

(1) Natural frequency and damping ratio

Exposing both the MRF and FDBF to white noise excitation, ranging from 0 Hz to 8 Hz, with a 2-mm amplitude and conducting Fourier transformation on the resultant acceleration data facilitated the determination of the natural frequencies of both structures through

frequency-response analysis. Subsequently, the damping ratios were determined using the half-power method based on the frequency-response function, as indicated in Table 2. The results revealed that the FDBF, equipped with friction energy-dissipating braces, exhibited higher damping ratios than the MRF, thereby improving its seismic resistance capabilities.

Table 2. Natural frequency and damping ratio.

Structure Model	Frame	FDBF
Natural frequency	3.1211 Hz	3.681 Hz
damping ratio	4.15%	4.77%

(2) Acceleration and displacement responses

The peak acceleration and displacement values for the top floor of both structures under seismic wave excitation are listed in Table 3. In the Y-direction, the FDBF exhibited reductions in peak acceleration values of 44.36%, 40.40%, 50.15%, and 48.75% compared to the MRF under the seismic waves of 1940 El Centro, 1979 El Centro, 1981 Salton Sea, and 1952 Taft, respectively. In the X-direction, these reductions were 29.3%, 27.5%, 9.09%, and 37.71%, respectively.

Table 3. Maximum top-floor acceleration and displacement.

Working Condition		1940 El Centro	1979 El Centro	1981 Salton Sea	1952 Taft	
Frame	X-direction	Acceleration/g	0.215	0.291	0.143	0.236
		Displacement/mm	29.32	35.12	26.61	27.11
	Y-direction	Acceleration/g	0.390	0.656	0.401	0.359
		Displacement/mm	30.86	34.12	27.47	27.12
FDBF	X-direction	Acceleration/g	0.152	0.211	0.130	0.147
		Displacement/mm	29.04	34.07	26.01	26.03
	Y-direction	Acceleration/g	0.217	0.391	0.168	0.184
		Displacement/mm	28.02	31	25.68	25.21
Displacement-reduction ratio	X-direction	/	0.96%	3.08%	2.31%	4.15%
	Y-direction	/	10.14%	9.14%	6.97%	7.58%

Figures 18 and 19 present the time history responses of the top-floor accelerations in the Y- and X-directions for both structures influenced by the four seismic waves. The FDBF displayed a significantly lower acceleration response in the Y-direction compared to the MRF, whereas its response in the X-direction was modestly reduced. This suggests that the friction energy-dissipating brace is highly effective in its implemented direction, with a less pronounced damping effect in the unbraced direction. The displacement-reduction ratio is defined as the ratio of the maximum top-floor displacement of the FDBF to that of the MRF. According to Table 3, the displacement-reduction ratios in the Y-direction are 10.14%, 9.14%, 6.97%, and 7.58%, and in the X-direction, they are 0.96%, 3.08%, 2.31%, and 4.15%, respectively. These findings indicate that the novel friction energy-dissipating brace significantly reduces the displacement response of the MRF, with a maximum reduction ratio reaching up to 10.14%. Figures 20–22 reveal that the displacements at each level of the FDBF are consistently lower than those of the MRF, with the ratio of inter-story displacement at each FDBF level being less than one.

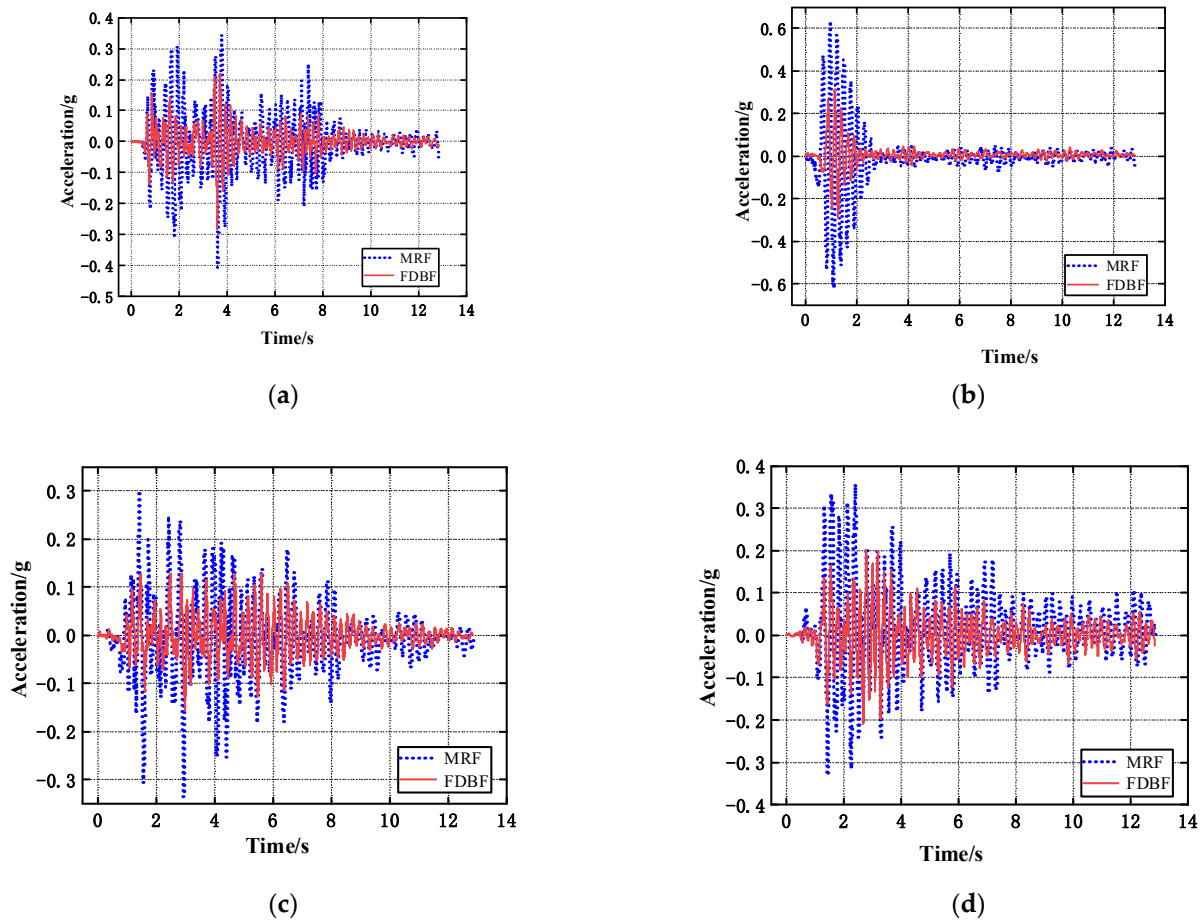


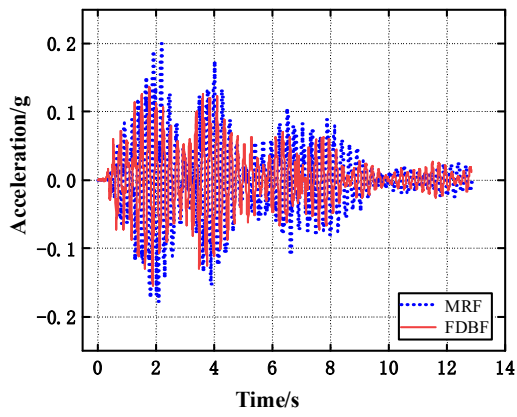
Figure 18. Acceleration–time histories of Y-direction seismic waves. (a) 1940 El Centro. (b) 1979 El Centro. (c) 1981 Salton Sea. (d) 1952 Taft.

(3) Acceleration amplification factor β

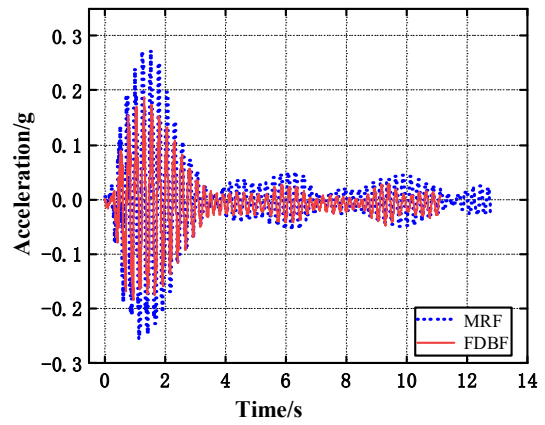
The acceleration amplification factor denotes the ratio of the maximum acceleration at the top of the structure to the maximum acceleration on the shaking table, illustrating the amplification effect of the top-floor acceleration during an earthquake. The data were collated, and the acceleration amplification factor in the Y-direction was calculated for both structures under the impact of four seismic waves; these findings are presented in Table 4. For comparative purposes, the acceleration amplification factor is plotted as a bar graph in Figure 23.

Table 4. Acceleration amplification factor β .

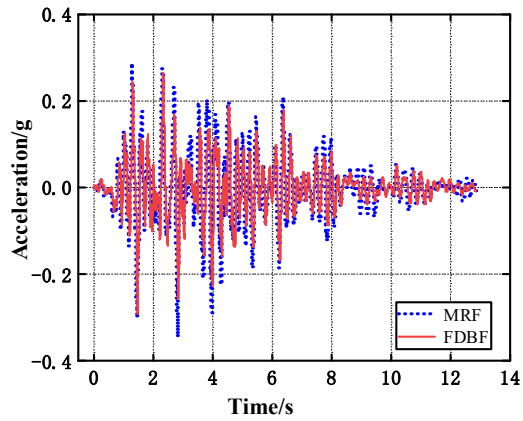
Earthquake	MRF			FDBF		
	Table Acceleration/g	Top-Floor Acceleration/g	β	Table Acceleration/g	Top-Floor Acceleration/g	β
1940 El Centro	0.176	0.390	2.22	0.172	0.217	1.26
1979 El Centro	0.255	0.656	2.57	0.219	0.391	1.78
1981 Salton Sea	0.192	0.401	2.09	0.213	0.398	1.73
1952 Taft	0.183	0.359	1.96	0.182	0.184	1.01



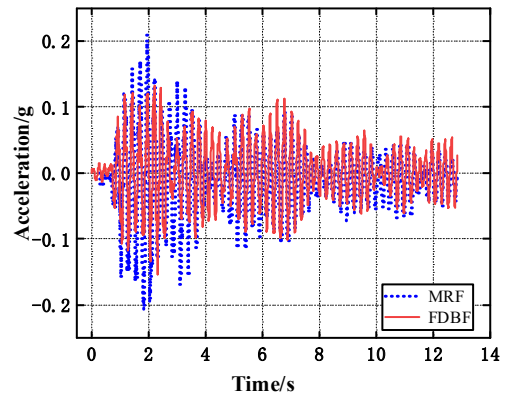
(a)



(b)

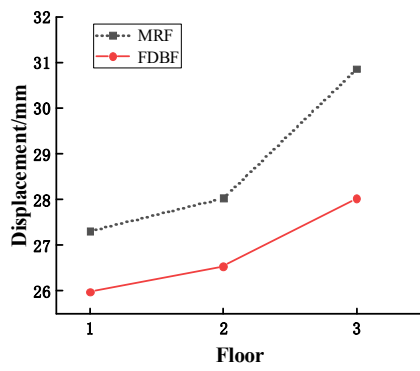


(c)

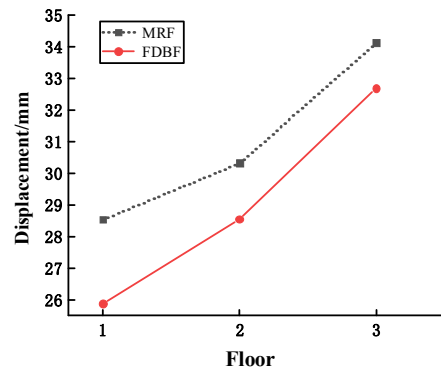


(d)

Figure 19. Acceleration–time histories of X-direction seismic wave. (a) 1940 El Centro. (b) 1979 El Centro. (c) 1981 Salton Sea. (d) 1952 Taft.

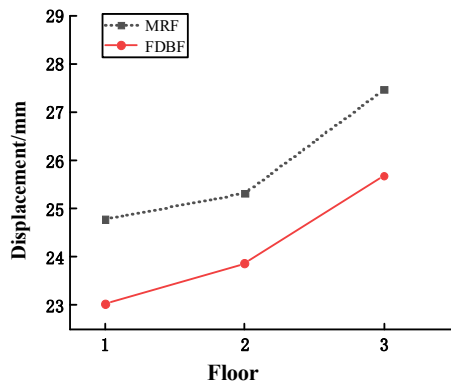


(a)

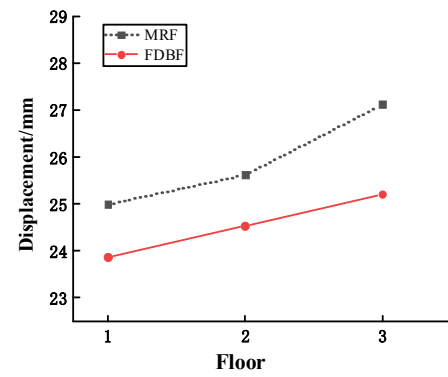


(b)

Figure 20. Cont.

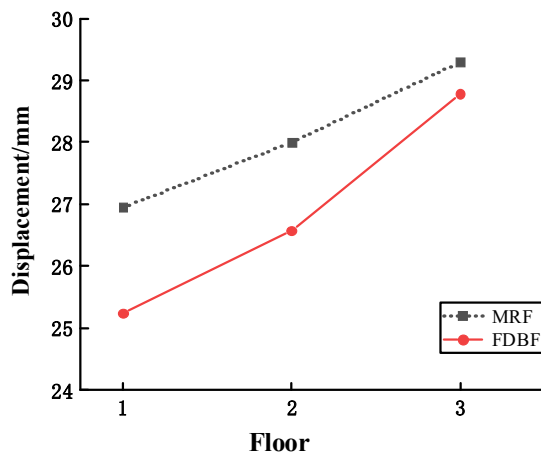


(c)

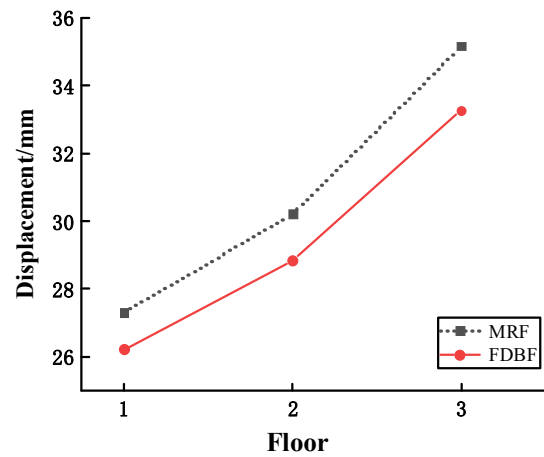


(d)

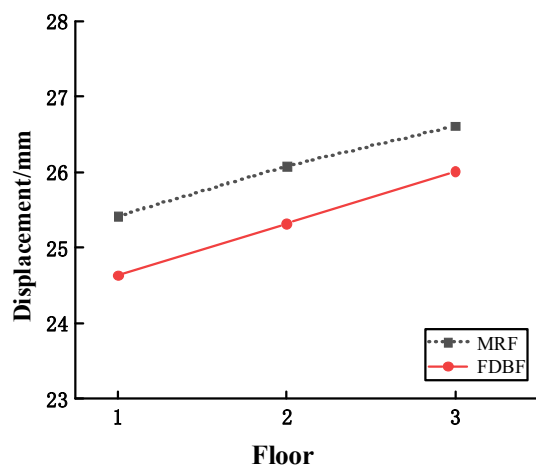
Figure 20. Maximum floor displacement of Y-direction seismic wave. (a) 1940 El Centro. (b) 1979 El Centro. (c) 1981 Salton Sea. (d) 1952 Taft.



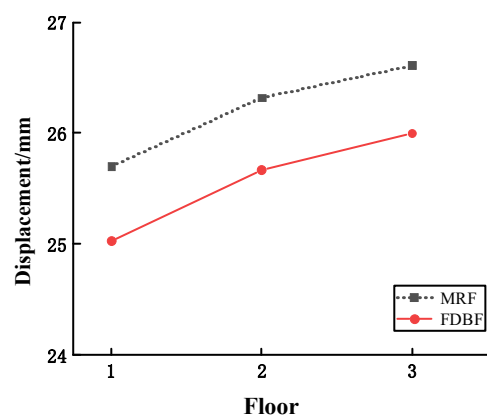
(a)



(b)



(c)



(d)

Figure 21. Maximum floor displacement of X-direction seismic wave. (a) 1940 El Centro. (b) 1979 El Centro. (c) 1981 Salton Sea. (d) 1952 Taft.

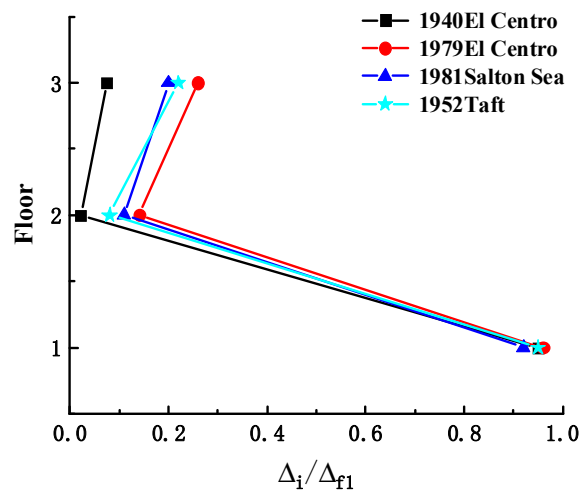


Figure 22. Ratio of inter-story displacement between each floor of FDBF and MRF on the first floor.

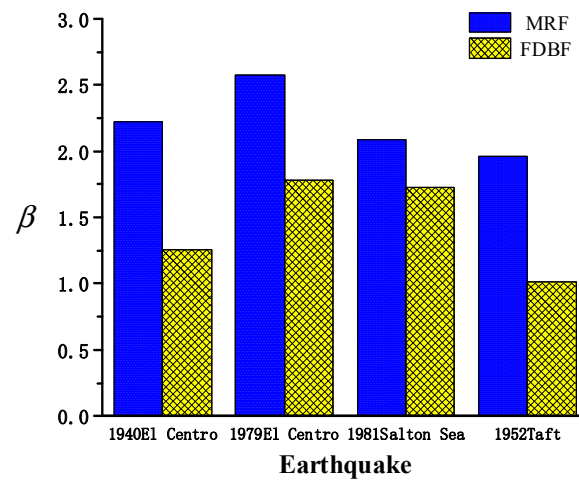


Figure 23. Acceleration amplification factor β .

Table 4 and Figure 23 reveal that the acceleration amplification factor of the FDBF is consistently lower than that of the MRF and remains below two. This observation highlights the crucial role of the friction energy-dissipating brace in mitigating seismic effects within the framed structure.

4. Finite Element Simulation

To comprehensively assess the seismic-reduction impact of the FDBF, the shaking-table test results were compared with finite element simulations conducted on the MRF, BMRF, and FDBF using ABAQUS 6.14 software. The acceleration–time and displacement–time responses of these three structures were contrasted under earthquake excitation, demonstrating the seismic mitigation efficiency of the FDBF.

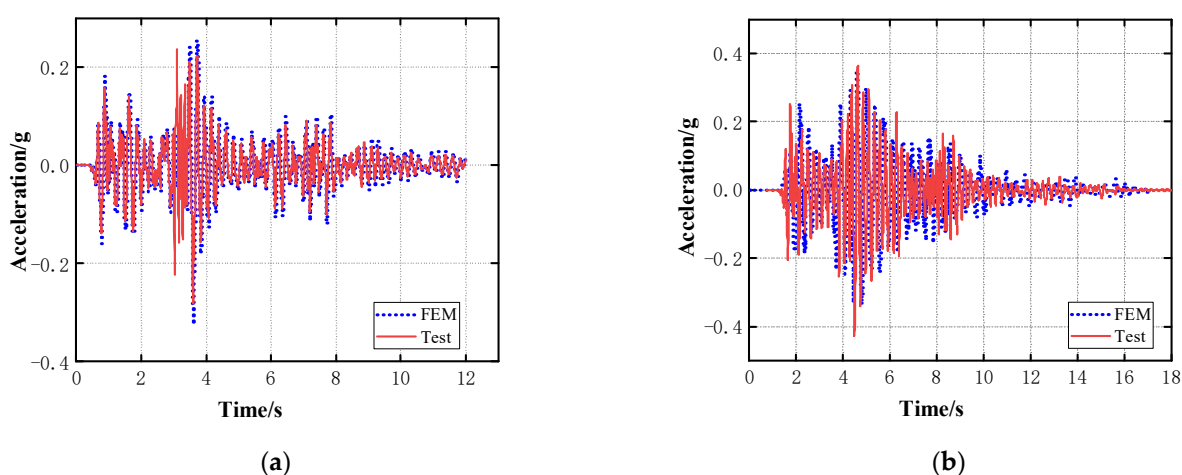
4.1. Finite Element Model Verification

Finite element models of both the experimental MRF and FDBF were developed in ABAQUS. A modal analysis was performed to determine the natural frequencies of the two structures. Table 5 presents a comparison between the simulated outcomes and experimental data, showing relative closeness with differences ranging from 2% to 5%. This suggests that the finite element model effectively replicates the experimental specimen.

Table 5. Comparison of natural frequencies (top three modes)/Hz.

Mode	MRF			FDBF		
	1	2	3	1	2	3
Test	3.121	3.334	5.15	3.681	3.892	6.061
Finite	3.046	3.257	5.061	3.503	3.798	5.996

After the modal analysis, damping parameters were incorporated into the models. The 1940 El Centro earthquake wave was then applied at the base of the structures, and the top-floor acceleration response in the Y-direction was compared with experimental results, as illustrated in Figure 24. The comparative analysis indicated commendable consistency in acceleration responses between the FDBF and MRF, demonstrating the proficiency of the finite element model in simulating the experimental model.

**Figure 24.** Comparison of acceleration–time histories (a) FDBF. (b) MRF.

4.2. Finite Element Model

The three model sets included the MRF, BMRF, and FDBF with energy-dissipating braces on each floor, as illustrated in Figure 25. The original structure was a five-story, one-span, center-supported steel-frame structure. The finite element models represented a scaled-down version of this prototype, focusing on a single five-story span. The column spacing in the X- and Y-directions was 450 mm and 540 mm, respectively, with a story height of 225 mm and a floor thickness of 2 mm. Columns and supports were modeled using beam elements, while floor slabs employed shell elements.

In the numerical model, the damper is using a full scale of the damping mechanism. The length and width of the damper connecting plates in the numerical model are the same as those in the experimental model. The thickness of the connecting plates and friction plates is 2 mm, different from the experimental model. This is due to the fact that the thickness of the slabs is different in the two models. Considering the connection installation between the braces and the floor slabs, different thicknesses are used. The damping devices were modeled with solid elements. The bases of the columns were fixed, eliminating displacements and rotations. The interaction between the friction pads and connectors was defined as surface-to-surface contact, employing penalized tangential contact and rigid normal contact. General contact was applied for interactions between other components. Except for the friction pads and high-strength bolts, Q345 steel was used for the model components.

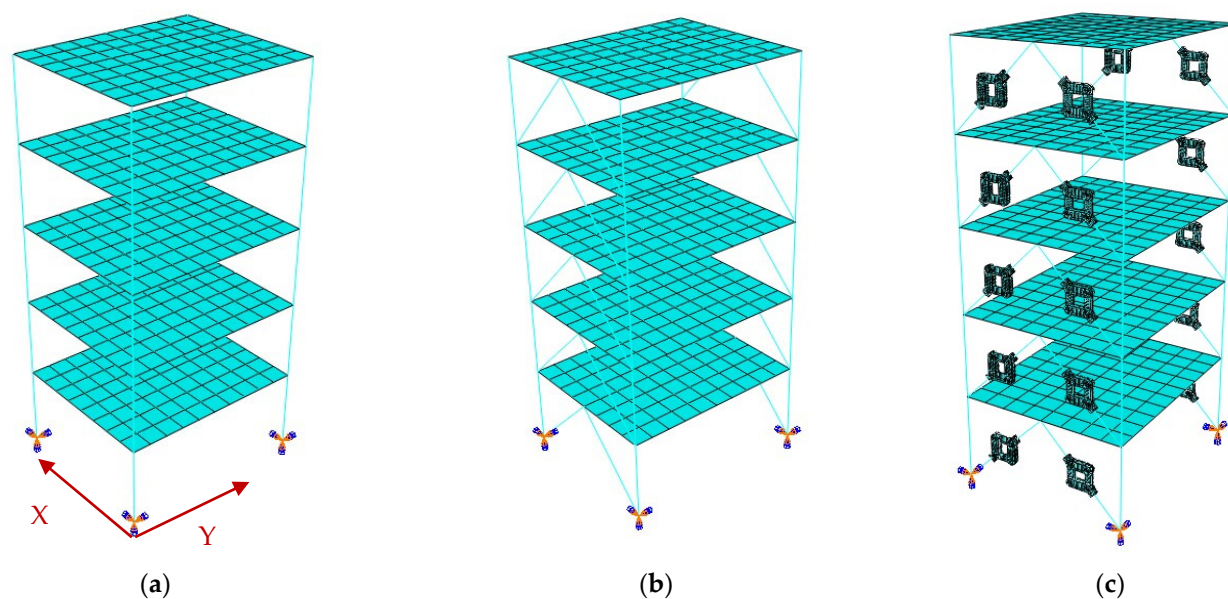


Figure 25. Different finite element models for various structures. (a) MRF. (b) BMRF. (c) FDBF.

4.3. Modal Analysis

Modal analysis was conducted on three structures: MRF, BMRF (ordinary braced frames), and FDBF. This analysis aimed to identify the mode shapes and frequencies for the top three modes. The specific frequencies for each mode are presented in Table 6. An examination of these results indicates that both the BMRF and FDBF exhibit higher frequencies compared to the MRF. Notably, the FDBF demonstrates lower frequencies than the BMRF, suggesting that the integration of the energy-dissipating brace alters the structural stiffness, which is beneficial for seismic energy dissipation relative to ordinary supports.

Table 6. Natural frequencies of MRF, BMRF, and FDBF (top three modes)/Hz.

Mode	1	2	3
MRF	1.227	1.243	1.706
BMRF	1.487	5.704	13.382
FDBF	1.476	5.611	13.256

4.4. Acceleration Response

Seismic waves, namely, the 1940 El Centro, 1979 El Centro, 1981 Salton Sea, and 1952 Taft earthquakes, were applied to the structural models. The peak accelerations for these waves were set to 0.21 g, 0.21 g, 0.19 g, and 0.18 g, respectively. The top-level acceleration–time history curves for these three structures are illustrated in Figure 26. The BMRF structure exhibited the highest acceleration response, followed by the MRF, whereas the base-isolated FDBF structure displayed the smallest acceleration response. Therefore, the novel friction energy-dissipating brace can effectively dissipate seismic energy and possesses significant damping properties.

To assess the amplification effect of top-level acceleration under identical seismic waves, the acceleration amplification factors of the models were calculated. The results are detailed in Table 7. The MRF displayed the highest amplification factor, followed by the BMRF, both exceeding 2.0, signifying a considerable amplification effect on the top-level acceleration in these structures. The base-isolated FDBF structure exhibited a maximum amplification factor of 1.17 and a minimum of 1.05, demonstrating its efficacy in reducing the top-level acceleration response and underscoring its damping capabilities.

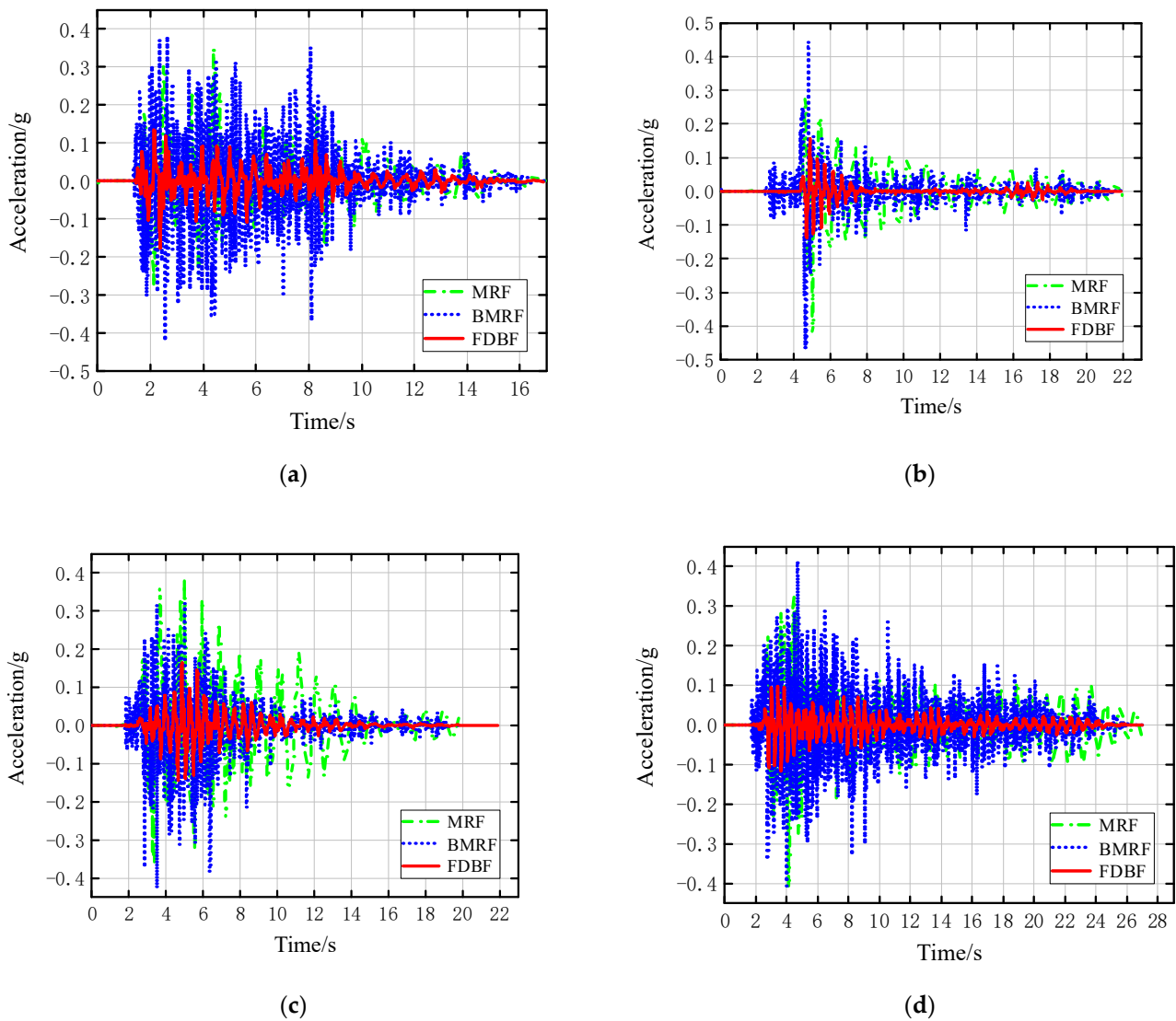


Figure 26. Comparison of acceleration–time histories of the three structures under seismic excitation. (a) 1940 El Centro. (b) 1979 El Centro. (c) 1981 Salton Sea. (d) 1952 Taft.

Table 7. Acceleration amplification factor β (acceleration unit (g)).

Earthquake	MRF			BMRF			FDBF		
	Ground Acceleration	Top-Level Acceleration	β	Ground Acceleration	Top-Level Acceleration	β	Ground Acceleration	Top-Level Acceleration	β
1940 El Centro	0.181	0.398	2.20	0.173	0.348	2.01	0.149	0.175	1.17
1979 El Centro	0.213	0.467	2.19	0.201	0.423	2.11	0.150	0.157	1.05
1981 Salton Sea	0.194	0.427	2.20	0.192	0.389	2.02	0.164	0.187	1.14
1952 Taft	0.180	0.414	2.30	0.179	0.403	2.25	0.166	0.176	1.06

Comparing the acceleration responses of the three structural models, the amplification factors from Table 6 are represented as a bar chart in Figure 27. As observed, the top-level acceleration-response peak of the FDBF structure, equipped with friction energy-dissipating braces, decreased by 40–50% compared to the MRF. The BMRF structure, with regular supports, achieved a decrease of approximately 15–25% compared to the MRF. Furthermore, the FDBF structure exhibited a reduction of approximately 35–50% compared to the BMRF structure. These findings demonstrate that the FDBF has a substantial vibration-damping effect.

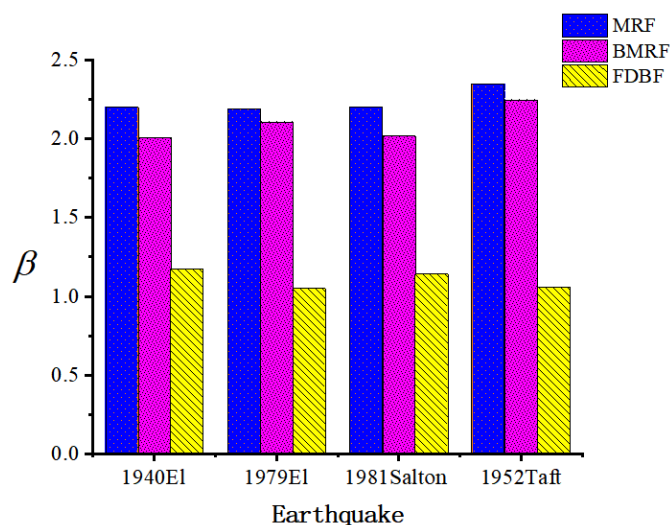


Figure 27. Acceleration amplification factors for the three structures.

4.5. Displacement-Reduction Rate α

The displacement-reduction rate is defined as the ratio between the maximum displacement of a seismically isolated structure and the maximum displacement of the same structure without isolation, typically a pure frame structure. This rate is crucial in assessing the seismic performance of the isolated structure, where a higher displacement-reduction ratio signifies improved damping efficacy and a smaller displacement response. To evaluate the seismic performance of both the BMRF and FDBF structures under various seismic excitations, a time history analysis was conducted using seismic waves with peak accelerations adjusted in accordance with the “Code for Seismic Design of Buildings GB50011–2010 (2016 Edition)” [36] for different design ground motion intensities. The peak accelerations were set to 0.14 g, 0.40 g, and 0.63 g, simulating SLE (Service-Level Earthquake) intensity 9, OBE (Operating Basis Earthquake) intensity 9, and MCE (Maximum Credible Earthquake) intensity 9, respectively. The structures were analyzed under these modified seismic waves.

Table 8 outlines the maximum displacement peaks and displacement-reduction ratios α for the FDBF, BMRF, and MRF under the influence of four different seismic waves with a peak acceleration of 0.14 g. Under SLE intensity 9, the displacement-reduction ratio of the FDBF structure is similar to that of the BMRF. This is primarily due to the fact that, during minor seismic events, the ordinary braces of the BMRF remain in an elastic state, and the friction dampers in the FDBF are not yet operational, rendering the energy-dissipating brace equivalent to an ordinary brace.

Table 8. Peak displacement (mm) of MRF, FDBF and BMRF (SLE intensity 9).

Working Condition	1940 El Centro	1979 El Centro	1981 Salton Sea	1952 Taft
MRF	7.08	10.75	8.06	7.33
FDBF	1.31	1.76	1.73	1.88
α /%	81.5	83.6	78.5	74.3
BMRF	1.23	1.66	1.72	1.99
α /%	82.6	84.6	78.7	72.8

Table 9 outlines the maximum displacement peaks and displacement-reduction ratios α for the FDBF, BMRF, and MRF under the influence of seismic waves with a peak acceleration of 0.40 g. Here, the displacement-reduction ratios of the BMRF are markedly lower than those of the FDBF under OBE intensity 9. This is due to the fact that, under OBE intensity 9, the new type of friction damper becomes active, and the energy-dissipating braces reduce structural displacement by absorbing seismic energy. Moreover, the ordinary

brace enters a compression-yielding state, leading to a significant decrease in the lateral stiffness of the structure and an increase in displacement.

Table 9. Peak displacement (mm) of MRF and FDBF (OBE intensity 9).

Working Condition	1940 El Centro	1979 El Centro	1981 Salton Sea	1952 Taft
MRF	12.74	19.35	14.51	13.19
FDBF	4.91	8.48	8.02	5.29
α /%	61.4	56.2	44.7	59.9
BMRF	8.37	12.72	12.03	7.94
α /%	34.2	34.3	17.1	39.8

Table 10 outlines the peak displacements and displacement-reduction ratios for the FDBF, BMRF, and MRF under rare earthquake conditions. The data indicate that the displacement-reduction ratios for the FDBF structure exceed 60% across various seismic wave excitations during rare earthquakes. The displacement reduction rate of the BMRF structure is consistently below 10%, with its maximum displacement essentially mirroring that of the MRF structure. This reflects the yielding of ordinary braces under MCE intensity 9. Conversely, the FDBF structure demonstrates effective damping effects owing to the operational friction dampers, exhibiting robust seismic mitigation performance.

Table 10. Peak displacement (mm) of MRF, FDBF and BMRF (MCE intensity 9).

Working Condition	1940 El Centro	1979 El Centro	1981 Salton Sea	1952 Taft
MRF	21.16	30.1	25.01	25.65
FDBF	7.44	8.99	8.73	8.98
α /%	64.8	69.9	65.1	65.0
BMRF	19.99	27.95	23.02	24.35
α /%	5.53	7.14	8.01	5.07

Figure 28 illustrates the peak displacements of the FDBF and MRF. The peak displacements of the FDBF are significantly smaller than that of the MRF under SLE, OBE and MCE intensity 9, and the reduction is more significant under MCE intensity 9. It shows that the FDBF shows good damping effect and the damping effect is better under rare earthquakes.

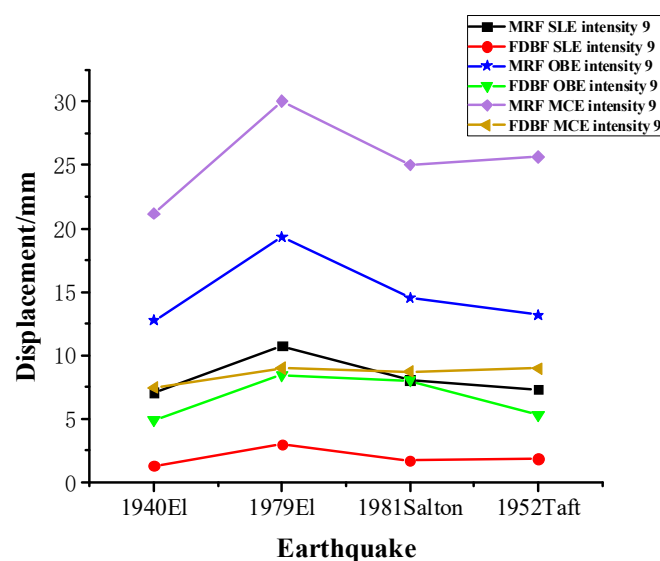


Figure 28. The peak displacements of the MRF and FDBF.

To illustrate the damping impact of the FDBF under earthquake conditions more effectively, the displacement reduction rates α from Tables 8–10 are visualized in Figure 29. As shown in the figure, at SLE intensity 9, the displacement reduction rates of both the FDBF and BMRF structures are similar, reflecting comparable seismic mitigation effects. At OBE intensity 9, the displacement reduction rate of the FDBF structure surpasses that of the BMRF structure. This difference arises as ordinary braces start to yield, leading to a decrease in stiffness. Concurrently, the new friction dampers become active, adjusting the brace length through their deformation to prevent brace compression. During MCE intensity 9, the BMRF structure loses nearly all of its seismic mitigation effectiveness owing to brace yielding and damage. In contrast, the displacement reduction rates of the FDBF structure exceed 60% as the deformations of the dampers in the energy-dissipating braces become more pronounced under severe seismic actions, effectively dissipating seismic energy and yielding superior seismic mitigation results.

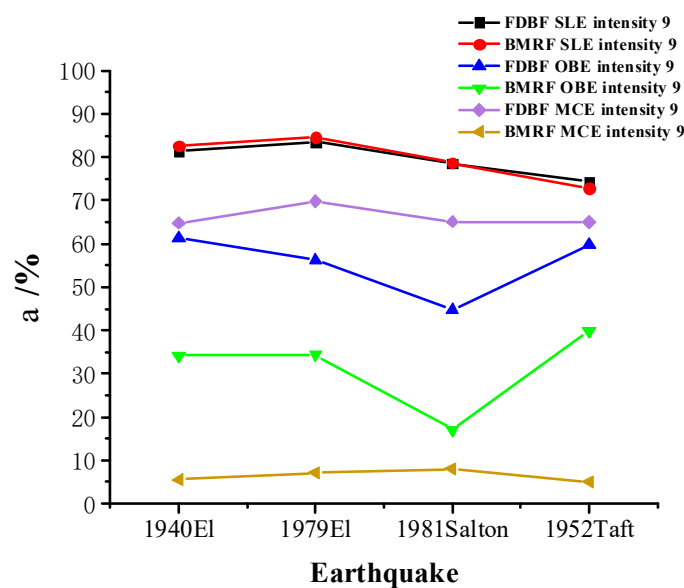


Figure 29. Displacement-reduction ratios α of the FDBF and BMRF.

5. Conclusions

A novel friction damper was proposed, and its hysteresis performance was examined. Shaking-table tests and finite element simulation analyses of the friction energy-dissipating braced frame structure, equipped with the new friction damper, were conducted. These tests evaluated the acceleration and displacement responses of the FDBF and MRF structures under seismic wave excitation. Finite element software enabled a comparative analysis of the seismic performance of the MRF, BMRF, and FDBF structures. The following conclusions were drawn:

- (1) The hysteresis curve of the new friction damper is predominantly rectangular and complete, showing no significant stiffness degradation after repeated loadings. This indicates a stable and efficient energy dissipation capacity.
- (2) Shaking-table tests revealed that the friction energy dissipation support at the bottom layer modified the dynamic characteristics of the original structure. Under seismic wave excitation, the peak acceleration at the top layer of the FDBF was reduced by 40–50% compared to the MRF, demonstrating a substantial seismic damping effect.
- (3) With identical seismic wave excitation, the amplification factor of the peak top acceleration for both the MRF and BMRF exceeded 2, whereas that for the FDBF ranged between 1.05 and 1.17. This suggests a more significant seismic damping effect in the FDBF structure compared to the BMRF structure. During SLE intensity 9 earthquakes, the displacement-reduction rate of the FDBF was comparable to that of the

BMRF. However, under OBE and MCE intensity 9 earthquakes, the energy dissipation capacity of the BMRF diminished due to brace yielding, whereas the displacement-reduction rate of the FDBF was between 45 and 61% and between 60 and 70% under OBE and MCE intensity 9 earthquakes, respectively. This demonstrates the effectiveness of FDBF in damping both OBE and MCE earthquakes, with superior seismic mitigation performance during rare earthquakes.

This study did not examine certain factors affecting the seismic performance of friction dissipative braced frame structures, such as the placement and number of friction dissipative braces and the threshold slip force of the new friction dampers. Subsequent research can delve into these aspects in greater depth to provide further insights into the engineering application of this system.

Author Contributions: Conceptualization, L.Y. and C.Z.; methodology, C.Z.; software, L.Y.; validation, L.Y. and C.Z.; formal analysis, L.Y. and C.Z.; writing—original draft preparation, L.Y.; writing—review and editing, L.Y. and C.Z.; funding acquisition, C.Z. All authors have read and agreed to the published version of the manuscript.

Funding: This research was financially supported by the Ministry of Science and Technology of China (Grant No. 2019YFE0112400), the Department of Science and Technology of Shandong Province (Grant No. 2021CXGC011204).

Data Availability Statement: The data presented in this study are available on request from the corresponding author. The data are not publicly available due to the research on this topic is continuing.

Conflicts of Interest: The authors declare no conflict of interest.

References

1. Zhou, F. Development and application of isolation, energy dissipation, and structural control technology. *World Earthq. Eng.* **1989**, *4*, 16–20.
2. Jaisee, S.; Yue, F.; Ooi, Y.H. A state-of-the-art review on passive friction dampers and their applications. *Eng. Struct.* **2021**, *235*, 112022. [[CrossRef](#)]
3. Weining, S.; Xueli, W.; Zhanfei, W. Experimental study on mechanical properties of the steel friction discs used in a rotational friction damper. *Structures* **2021**, *29*, 1808–1818.
4. Pall, S.A.; Marsh, C. Response of friction damped braced frames. *J. Struct. Div. ASCE* **1982**, *108*, 1313–1323. [[CrossRef](#)]
5. Pall, S.A.; Marsh, C.; Fazio, P. Friction joints for seismic control of large panel structures. *PCI J.* **1980**, *25*, 38–61. [[CrossRef](#)]
6. Filiatrault, A.; Cherry, S. Performance evaluation of friction damped braced steel frames under simulated earthquake loads. *Earthq. Spectra* **1987**, *3*, 57–78. [[CrossRef](#)]
7. Chen, Z. Experimental research of a new type of energy dissipating bracing. *J. Build. Struct.* **1989**, *10*, 23–31.
8. Valente, M. Friction damper devices for seismic performance improvement of steel frames. *Int. Conf. Adv. Steel Struct.* **2012**, *1*, 58–70.
9. Wei, L.W.L. Study on table shaking test of RC frame model with friction energy-dissipation bracings. *J. Build. Struct.* **1997**, *18*, 29–37.
10. Hashemi, A.; Bagheri, H.; Zarnani, P.; Quenneville, P. Seismic performance of friction-damped steel frames integrated with resilient tension-only braces. *J. Constr. Steel Res.* **2021**, *176*, 106381. [[CrossRef](#)]
11. Zhou, Y. New Technology and System for Energy Consumption and Seismic Reduction in Buildings. PhD Thesis, Harbin Architecture University, Harbin, China, 1996.
12. Zhang, C.W. The active rotary inertia driver system for flutter vibration control of bridges and various promising applications. *Sci. China Technol. Sci.* **2023**, *66*, 390–405. [[CrossRef](#)]
13. Colajanni, P.; Papia, M. Seismic response of braced frames with and without friction dampers. *Eng. Struct.* **1995**, *17*, 129–140. [[CrossRef](#)]
14. Xian, Q. The Theoretical and Experimental Research on Energy Dissipating Brace Frame Structures. PhD Thesis, Hunan University, Changsha, China, 2000.
15. Naem, A.; Kim, J. Seismic retrofit of structures using rotational friction dampers with restoring force. *Adv. Struct. Eng.* **2020**, *23*, 3525–3540. [[CrossRef](#)]
16. Wu, B.; Zhang, J.; Ou, J. Experimental study and numerical analysis of Pall friction damper. *J. Build. Struct.* **2003**, *24*, 7–13.
17. Ghasemi, M.; Zhang, C.; Khorshidi, H.; Zhu, L.; Hsiao, P.-C. Seismic upgrading of existing RC frames with displacement-restraint cable bracing. *Eng. Struct.* **2023**, *282*, 115764. [[CrossRef](#)]
18. Sheldon, C.; Yeda, L.; Xunan, Z. Damping characteristics of friction-damped braced frame and its effectiveness in the mega-sub controlled structure system. *Earthq. Eng. Eng. Vib.* **2007**, *6*, 171–181.

19. Liu, W.; Lian, W.; Li, S. Friction Dampers and Friction Damped Braced Frames. *J. Nanjing Archit. Civ. Eng. Inst.* **1994**, *29*, 9–16.
20. Wen, B.-P.; Zang, F.-C.; Zhang, H.-L.; Yang, D.L.; Wei, Y.H.; Chen, Y. Study on the seismic performance of a new type rotational friction damper. *Earthq. Resist. Eng. Retrofit.* **2022**, *44*, 76–81.
21. Mualla, I.H.; Belev, B. Analysis, design and applications of rotational friction dampers for seismic protection. *Arch. J. Civ. Eng. Env. Arch.* **2016**, *62*, 335–346. [[CrossRef](#)]
22. Xiaoqi, Y.; Yan, W.; Haibin, Z.; Liwei, M. Experimental study on hysteretic performance of rotating friction damper. *Ind. Arch.* **2020**, *50*, 151–157.
23. Javidan, M.M.; Kim, J. Seismic retrofit of soft-first-story structures using rotational friction dampers. *J. Struct. Eng.* **2019**, *145*, 04019162. [[CrossRef](#)]
24. Wei, G.; Hengchao, X. Performance of a novel rotational frictional damper. *Struct. Eng.* **2018**, *34* (Suppl. S1), 54–58.
25. Wei, G.; Chen, Z.; Xu, X.; Dan, B. Pseudo dynamic Hybrid Simulation of High-Speed Railway Bridge-Track System with Rotational Friction Damper. *Int. J. Struct. Stab. Dyn.* **2020**, *20*, 2040014.
26. Kim, J.; Choi, H.; Min, K.W. Use of rotational friction dampers to enhance seismic and progressive collapse resisting capacity of structures. *Struct. Des. Tall Build.* **2011**, *20*, 515–537. [[CrossRef](#)]
27. Monir, H.S.; Zeynali, K. A modified friction damper for diagonal bracing of structures. *J. Constr. Steel Res.* **2013**, *87*, 17–30. [[CrossRef](#)]
28. Wang, G.; Wang, Y.; Yuan, J.; Yang, Y.; Wang, D. Modeling and experimental investigation of a novel arc-surfaced frictional damper. *J. Sound. Vib.* **2017**, *389*, 89–100. [[CrossRef](#)]
29. Soong, T.T.; Skinner, G.T. Experimental study of active structural control. *J. Engrg Mech. Div.* **1981**, *107*, 1057–1067. [[CrossRef](#)]
30. Spencer, B.F.; Dyke, S.J.; Deoskar, H.S. Benchmark problems in structural control: Part I—Active Mass Driver system. *Earthq. Engng Struct. Dyn.* **1998**, *27*, 1127–1139. [[CrossRef](#)]
31. Agrawal, A.K.; Nagarajaiah, S. Benchmark structural control problem for a seismically excited highway bridge: Phase I and II. *Struct. Control Health Monit.* **2009**, *16*, 503–508. [[CrossRef](#)]
32. Spencer, B.F.; Dyke, S.J.; Deoskar, H.S. Benchmark problems in structural control: Part II—Active tendon system. *Earthq. Engng Struct. Dyn.* **1998**, *27*, 1141–1147. [[CrossRef](#)]
33. Chin Hsiung, L.; Mualla, I.; Liao, W.I. Shaking-table test of a friction-damped frame structure. *Struct. Des. Tall Spec. Build.* **2004**, *1*, 13.
34. Wengang, Z.; Songshan, N.; Fei, P.; Yiqian, C. Selection of input ground motions for seismic fragility analysis considering structural nonlinear response. *J. Dyn. Control* **2023**, *21*, 80–86.
35. Mirzabagheri, S.; Sanati, M.; Aghakouchak, A.A.; Khadem, S.E. Experimental and numerical investigation of rotational friction dampers with multi units in steel frames subjected to lateral excitation. *Arch. Civ. Mech. Eng.* **2015**, *15*, 479–491. [[CrossRef](#)]
36. GB50011–2010; Code for Seismic Design of Buildings (2016 Edition). Construction Industry Press: Beijing, China, 2016.

Disclaimer/Publisher’s Note: The statements, opinions and data contained in all publications are solely those of the individual author(s) and contributor(s) and not of MDPI and/or the editor(s). MDPI and/or the editor(s) disclaim responsibility for any injury to people or property resulting from any ideas, methods, instructions or products referred to in the content.